Heliyon 9 (2023) e16081

Contents lists available at ScienceDirect

Heliyon

journal homepage: www.cell.com/heliyon

Research article

ZnS:Eu @ZIF-8: Selective formation of ZnS:Eu QDs within a zinc methylimidazole framework for chemical sensing applications

Qian Wang, Hongtao Chu *, Jingru Zhang, Wenhui Ma, Shili Qin, Lidi Gao

College of Chemistry and Chemical Engineering, Qiqihar University, Qiqihar, China

ARTICLE INFO

Keywords:
MOFs
ZnS
Eu
Photoluminescence
Fluorescent probes
TNP

ABSTRACT

Light harvesting based on a microporous zeolite imidazole backbone (MOF) has attracted considerable interest as a fluorescent sensor for the detection of analytes. In this work, we have prepared a novel complex containing quantum dots of doped rare earth elements by a one-pot method. to be applied to the fluorescence detection of pollution hazards. Because of the solid framework, the prepared ZnS:Eu@ZIF-8 composite shows desirable fluorescence properties. The selectivity and sensitivity of ZnS:Eu@ZIF -8 to TNP, which has a detection limit of 0.19 μmol/L, is further investigated and its sensing mechanism is discussed by means of fluorescence lifetime measurements in combination with emission and UV spectra. It should also be noted that this is the first doped quantum dot to be encapsulated in a MOF to be used for the potential detection of phenolic compounds in the aqueous environment, while the framework remains in place and no structural changes have occurred.

1. Introduction

Metal-organic frameworks [1] (MOFs) are highly ordered nanoporous networks derived from metal centres bonded with the terminal double coordination groups of organic molecules. They are an excellent class of carriers that are attracting increasing attention because of their high porosity and chemical stability. Composites can be prepared by combining MoFs with other components. However, a number of conditions must be met before MOF devices can be commercially realised: the spatial control of crystal growth on custom substrates, the scaling up of MOF production quickly and cheaply and the preparation of new host–guest framework composites containing functional species. These features make MOFs promising for a variety of applications, including gas storage, chemical separation and drug delivery. By acting as unique hosts for a variety of functional species, MOFs also offer the opportunity to develop novel types of composites that show enhanced (gas storage) or novel (catalytic, optical and conductive) behaviours [2–4]. Given their potential advantages, metal–organic backbones conferred with fluorescent properties are applied to detect some substances.

In this work, nanoparticles, i.e. QDs fluorescent materials, were encapsulated into MOFs to synthesise MOF-based composites, where the porous properties of MOFs can be combined with the fluorescent properties of quantum dots (QDs) [5,6], i.e. combining the advantages of the host and guest materials. MOF materials alone and high-performance light-emitting materials show a low quantum yield, which is detrimental to their practical application; however, this drawback can be overcome by combining these materials to improve their fluorescence sensing performance significantly [7]. A review of MOF-based host–guest systems in previous studies

* Corresponding author.
E-mail addresses: wq199705129@163.com (Q. Wang), lange19790@163.com (H. Chu).

https://doi.org/10.1016/j.heliyon.2023.e16081
Received 9 December 2022; Received in revised form 27 April 2023; Accepted 4 May 2023
Available online 9 May 2023

showed that researchers had focused primarily on developing materials with potential catalytic or gas storage applications. All these reported systems have a common element, namely, the introduction of metal (Pt, Pd, Ru or Cu) or metal oxide (TiO_2 or ZnO) nanoparticles into MOF crystals. The properties based on PXRD, TGA and luminescence measurements suggested that MOFs can be used as potentially versatile luminescent materials for the sensing of metal ions, anions and small organic molecules. In this study, pre-synthesised QDs were encapsulated into MOFs. However, where controlling the size and shape of the nanoparticles is crucial [8]. Fluorescence emission spectra can be adjusted by changing the size of the QDs and introducing dopant ions [9], the luminescence intensity of ZnS itself is too low to meet the luminescence requirements of the material in practical applications, and therefore, this work utilised elemental doping to improve the luminescence performance of ZnS to broaden its application areas [10–13].

Fluorescence spectroscopy detection technology has the advantages of fast real-time response, high-resolution [14], high sensitivity [15] and easy operation, and ratiometric fluorescent probes can overcome some environmental factors, such as changes in pH, fluorescence self-quenching and interference from background signals [16–20]. In addition to retaining the advantages of ordinary fluorescence spectroscopy, this technology has the advantages of simplified spectra, narrowed bands and scattered light reduction. Therefore, it has been used for the analysis of conformational changes in proteins. In this study, we designed a ratiometric fluorescent probe whose signal parameter is the ratio of the fluorescence emission intensity at two different wavelengths. Ratiometric fluorescent probes are of great importance, with the advantages of fast response, high selectivity and sensitivity, independence from pH [21] and a considerably broadened dynamic range. In this study, ZnS:Eu QDs were chosen to improve test selectivity and sensitivity, and the surface modification of the surfactant polyethene glycol was performed to obtain a ratiometric fluorescent probe encapsulated in a ZIF-8 framework.

ZnS is a broad-band semiconductor material with an intrinsic band gap free of toxic elements, such as Cd and Se; good biocompatibility; low toxicity; environmental friendliness and low cost. Therefore, it is considered to be an ideal alternative material. However, ZnS has a narrow luminescence spectrum and is susceptible to oxidation or decomposition; these characteristics lead to its low luminescence efficiency, which limits its widespread use in everyday production. Therefore, in an approach that improved the luminescence efficiency and stability and expanded the luminescence spectral range of ZnS, ion doping was performed to alter its carrier relaxation process to expand the application of ZnS nanomaterials [22]. In 2011, Tiwari [23] reported the effect of a capping agent on the absorption and photoluminescence (PL) spectra of ZnS:Cu nanocrystals. A blue shift of the absorption peak was observed and attributed to quantum confinement effects, which increased band gap energy. The PL spectra of the capped ZnS:Cu nanocrystals showed broad peaks in the 460–480 nm range. In 2010, Ma et al. [24] synthesised water-soluble ZnS and ZnS:Mn QDs coated with thioglycolic acid by using a hydrothermal method. The QDs were 4 nm in size and had a highly homogeneous morphology. The corresponding PL in the luminescence spectra was located at 420 nm for ZnS QDs and 580 nm for ZnS:Mn QDs. Water-soluble ZnS:Mn QDs have strong yellow light emission, are nontoxic to life and the environment and can be used as biofluorescent probes in lieu of CdSe and CdS materials. In 2014, Reddy et al. [25] investigated the synthesis of Mg-doped ZnS nanospheres by using a mixture of ethylenediamine and deionised water in the absence of any indicated active agent. Depending on the Mg content, blue-green PL with tuneable intensity and peak position was observed, and the Mg2+-activated ZnS phosphor can be well used as a blue-green component in near-UV white-light-emitting diodes.

2,4,6-trinitrophenol [26] (TNP, also known as picric acid) is widely used as a precursor in the synthesis of fireworks, explosives and fuels, and is highly toxic and explosive. In nitro explosives, TNP has a higher explosive power than TNT and even exceeds that of 2,4,6-trinitrotoluene. Its excessive use causes serious environmental contamination, especially in groundwater and soil, and not only that, but long-term human exposure can cause headaches; A huge threat to environmental health and military security [27]. Sometimes it causes peripheral neuritis [28], bladder irritation, and liver and kidney damage [29]. Therefore, there is an urgent need to establish a rapid and sensitive method to detect TNP in the environment, which is important not only for eliminating health hazards but also for protecting environmental issues. To date, methods for detecting picric acid include mass spectrometry [30], high performance liquid chromatography [31], gas chromatography [32], surface-enhanced Raman spectroscopy [33], electrochemical methods [34] and colorimetric methods [35] Methods for detecting TNP are complex or time-consuming and involve complex operation of expensive instruments, thus hindering their widespread use According to the current state of research, the detection of phenolic compounds relies mainly on expensive and sophisticated machines, it was found that high selectivity and sensitivity could be obtained by using fluorescence for the detection of such compounds.

2. Materials and methods

2.1. Instrumentation

Transmission electron microscopy images were recorded on a transmission electron microscope (H7650) from Hitachi with an acceleration voltage of 300 kV. A scanning electron microscope (S3400) with an energy dispersive spectrometer was used to obtain scanning electron microscopy (SEM) images and element-specific energy spectra.

While fluorescence spectra were obtained by applying an FL-S920 spectrophotometer (UK) under excitation at 350 nm, powder spectra were obtained by using an X-ray diffraction (XRD) Figure diffractometer (D8) from Bruker AXS, Germany. The slit width emission wavelengths were set to 3.0 or 5.0 nm for both excitations.

2.2. Experimental section

All chemicals were used directly after purchase from commercial corporations without further purification. Ultrapure water (18.2

MΩ cm) provided by a Purifier water purification system was used throughout all of the experiments.

Synthesis of QDs. QDs of different concentration percentages were prepared in accordance with the reported method [36]. Polyethene glycol (400) was used as a stabiliser to establish an efficient, accurate and sensitive fluorescence method. In brief, 1 M zinc acetate was mixed with 50 mL of methanol and 2 mL of polyethene glycol while stirring (400 rpm) at 27 °C for 10 min. Next, 50 mL of sodium sulphide (0.1 M) solution was added to the zinc solution and kept at 80 °C for 6 h during continuous stirring (700 rpm). The resulting precipitate was then washed with ethanol and Milli-Q water by using a centrifuge. The obtained precipitate was annealed at 100 °C (vacuum) for 12 h. Similarly, 1 M zinc acetate and europium chloride (2, 4 and 6 at%) were mixed in 50 mL of methanol and 2 mL of PEG while being stirred (400 rpm) at 27 °C for 10 min. The subsequent procedure was similar to that described above.

Synthesis of fluorescent probes. ZnS:Eu@ZIF-8 complexes of different concentration percentages were prepared through the one-pot method [37]. QDs containing different contents of doped Eu^{3+} were poured into a mixture containing zinc and dimethylimidazole solutions and reacted at room temperature for 24 h. The complexes were then obtained through centrifugation at 10000 rpm for 5 min and washed three times with methanol until the supernatant was free of fluorescence, then dried overnight in an oven at 60 °C. Finally, the ZnS:Eu@ZIF-8 composites were dispersed in ultrapure water and used for further analytical tests.

3. Results and discussion

3.1. XRD characterisation

•ZnS:Eu@ZIF-8 complexes were synthesised. The crystal structures of the synthesised ZnS:Eu@ZIF-8 and ZIF-8 were characterised by using XRD. The results of their characterisation are shown in Fig. 1. XRD revealed that the synthesised ZIF-8 had a cubic sodium-squaredite-related crystal structure. The peaks in the XRD pattern of ZIF-8, the MOF prepared in this experiment, were consistent with the reported diffraction peaks with the XRD diffraction angles of 5.42°, 10.12°, 12.5°, 15°, 16.22° and 17.52° corresponding to the crystal planes of (001), (002), (112), (022), (013) and (222), respectively. The grain size of ZnS:Eu quantum dots is 1.24 nm (As shown in Table 1),However, as far as the data is concerned, the diffraction intensity of this measured XRD data is very low and the error in the calculation may be a little larger. These findings were consistent with the reported structure of ZIF-8, demonstrating that the encapsulation of ZnS:Eu QDs into MOFs did not affect the crystal integrity of the carriers and indicating that ZIF-8 was synthesised successfully [38–42]· Moreover, the diffraction peaks of the ZnS:Eu@ZIF-8 composites were similar to those of pure ZIF-8. The figure shows that the synthesised ZIF-8 (Zn) had no other spurious peaks and low doping. This pattern indicated that the synthesised ZnS:Eu@ZIF-8 and ZIF-8 have high crystallinity and good purity.

Grain size calculations are based on the Debye Scherrer formula, as shown in Table 1 :

Where K is a constant, λ is the X-ray wavelength in nm, β is the specimen half-height width in rad, and θ is the half-diffraction angle in rad.

3.2. FTIR analysis

Fig. 2 provides the FTIR spectra of ZIF-8, ZnS:Eu QDs and ZnS:Eu@ZIF-8 complexes based on the ZIF-8 sample synthesised in this experiment. The characteristic absorption bands of the imidazole ring at 3134 and 2927 cm^{-1} were attributed to the stretching vibrational absorption peak of the C–H bond, and the peak at 1422 cm^{-1} originated from the stretching vibrational peak of C═N. The hydroxyl stretching vibration peak of ZIF-8 at 3403 cm^{-1} had disappeared, suggesting that the hydroxyl oxygen in ZIF-8 had

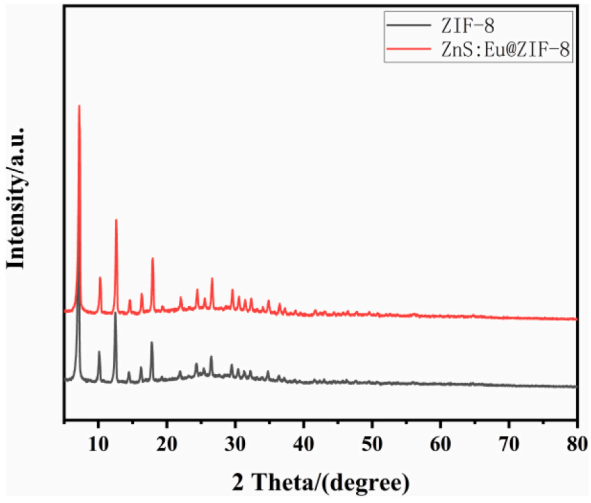

Fig. 1. Powder XRD plots of ZIF-8 (black) and ZnS:Eu@ZIF-8 QDs@ZIF-8 (red). (For interpretation of the references to color in this figure legend, the reader is referred to the Web version of this article.)

Table 1
Parameters of grain size.

K	λ(Å)	2θ(degree)	β(degree)	D (nm)
0.94	1.54178	22.35	6.821	1.2409
0.94	1.54178	28.621	7.311	1.17216
0.94	1.54178	48.422	4.929	1.84714
0.94	1.54178	57.294	13.181	0.71785

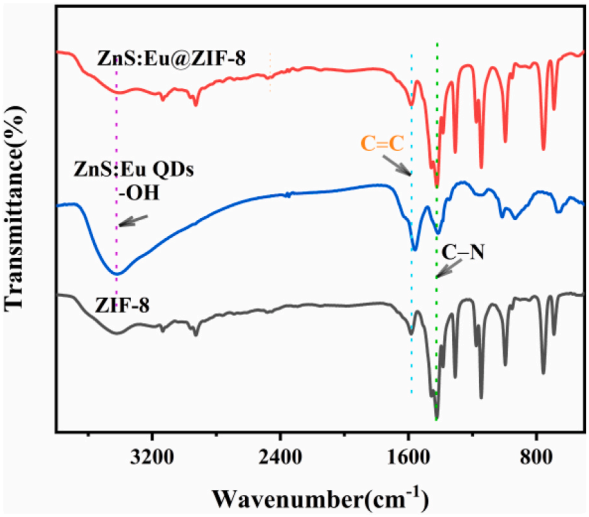

Fig. 2. FTIR spectra of ZnS:Eu@ZIF-8, ZnS:Eu QDs and ZIF-8.

coordinated with Eu^{3+} in the QDs, where the similarity between the main characteristic peaks of the IR spectra of ZnS:Eu@ZIF-8 and ZIF-8 seen in the figure [43] was due to the encapsulation of ZnS:Eu within the MOF. The small amount of ZnS:Eu was assumed not to affect the bonding between ZIF-8. However, the hydroxyl stretching vibration peak of ZIF-8 at 3403 cm^{-1} disappears, suggesting that the hydroxyl oxygen in ZIF-8 is coordinated to Eu^{3+} in the quantum dot.

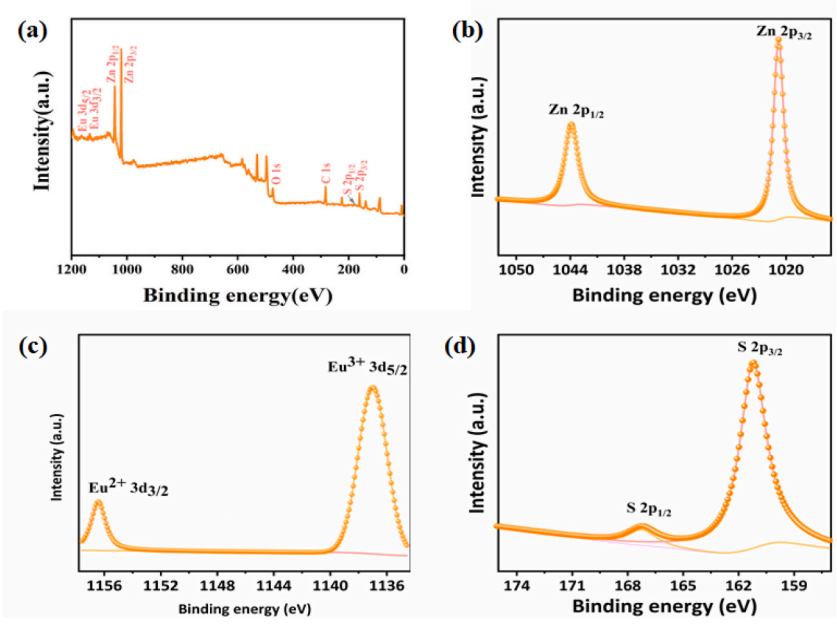

Fig. 3. XPS survey scan of ZnS:Eu (4%) QDs and ZnS:Eu (4%) QDs. (b–d) High-resolution XPS scans of Zn 2p, Cd 3d and S 2p.

3.3. XPS analysis

The ZnS:Eu QDs samples were further analyzed by X-ray electron spectroscopy (XPS) and it can be seen from Fig. 3(a) that the QDs consist of Zn, Eu, S, C and O. Fig. 3(b) shows a narrow scan of Zn, where two distinct spikes are seen to be emitted at wavelengths of 1043eV and 1020eV, belonging to Zn $2p_{1/2}$ and Zn $2p_{3/2}$, respectively. Fig. 3(c) shows a narrow scan of europium, belonging to $3d_{5/2}$ of Eu^{3+} at 1137eV, and the presence of Eu in a different valence state, Eu^{2+}, is also found at 1157eV , $3d_{3/2}$ belonging to Eu^{2+}.high-resolution XPS Two fitted peaks, 167eV and 161eV, belonging to S $2p_{1/2}$ and S $2p_{3/2}$, respectively, appear in the spectrum (Fig. 3(d)). The results demonstrate that the energy spectrum scans of the ZnS:Eu QDs are consistent with those reported in the literature [36], indicating that the QDs were synthesised successfully and can be used for the next step of encapsulation.

The elemental composition of ZnS:Eu@ZIF-8 was further explored through XPS. The full spectrum in Fig. 4(a) clearly illustrates that this complex was composed of the elements Zn, Eu, S, C, N and O. Fig. 4(b) shows a narrow scan of Zn, wherein the two most prominent peaks seen in the wavelength region at 1044.48 and 1021.28 eV belonged to the divalent Zn elements Zn $2P_{3/2}$ and Zn $2P_{1/2}$. Fig. 4(c) depicts peaks with the binding energies of 1146.18 and 1134.98 eV assigned to Eu $3d_{3/2}$ and Eu $3d_{5/2}$, respectively. Fig. 4(d) depicts a narrow XPS scan of S wherein S was divided into two peaks: S $2p_{3/2}$ (160.98 eV) and S2p1/2 (163.98 eV) compared to the absence of divalent Eu^{2+} in the doped QDs after cladding, indicating the high purity of the sample.

3.4. Electron microscopy characterisation

The morphologies of ZnS:Eu@ZIF-8 and ZnS:Eu QDs were analyzed by using SEM. Fig. 5(b) and (d) show that the ZnS:Eu QDs were uniformly dispersed with an average quantum size of approximately 6.3 nm. The SEM images illustrated that after the ZnS:Eu QDs were encapsulated into ZIF-8, as shown in Fig. 5(a) the morphology of the complex remained unchanged and was still a dodecahedral structure that could be seen as a solid inside the dodecahedron. The distribution of Zn, Eu, S, C and N in a single sample was tested by using EDX. The presence of Eu in this complex is illustrated in Fig. 5(c), indicating the successful synthesis of the fluorescent probe.

3.5. PL properties

The emission spectrum of ZnS:Eu@ZIF-8 was investigated to improve our understanding of the probe. The complexation of photogenerated charge pairs can release energy to induce PL. Therefore, the PL emission spectra of the semiconductor materials were recorded at an excitation wavelength of 226 nm to investigate the separation efficiency of the photogenerated electrons. Fig. 6(a) shows that the emission peaks of the complexes appeared at 437 and 658 nm. The free ligand dimethylimidazole exhibited strong fluorescence emission at 437 nm for Zn^{2+} defect luminescence. In the deep electron trap at 658 nm, attributed to the luminescence of the doped Eu^{3+}, the fluorescence emission peak was ascribed to the characteristic luminescence of the $^5D_0$-^7F_J (J ¼ 0, 1, 2) leap of Eu^{3+} [44]. It is worth noting that , A narrow emission peak at 483 nm appears, mainly due to a fringe effect caused by defective luminescence of Zn^{2+} at 437 nm. It is speculated that the band gap of the conjugated π-domain is considered to be the intrinsic emission centre. The defective luminescence of Zn^{2+} attributed to the deep electron trap triggers more emission sites, which leads to red-shifted emission. ZnS:Eu@ZIF-8 exhibited blue fluorescence, as illustrated in the CIE plot in Fig. 6(b). Given that the human eye is sensitive to

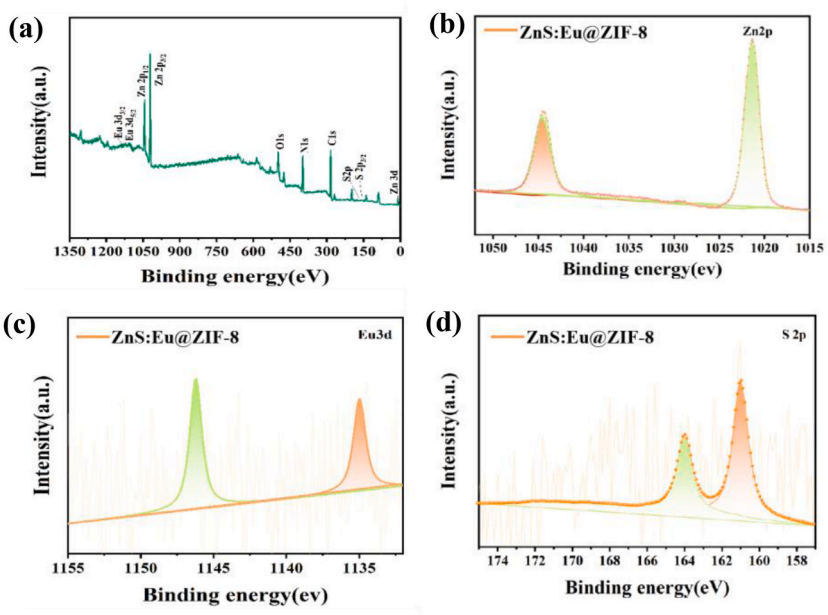

Fig. 4. XPS scans of ZnS:Eu (4 at%)@ZIF-8 complexes; (b–d) high-resolution XPS scans of Zn 2p, Cd 3d and S 2p.

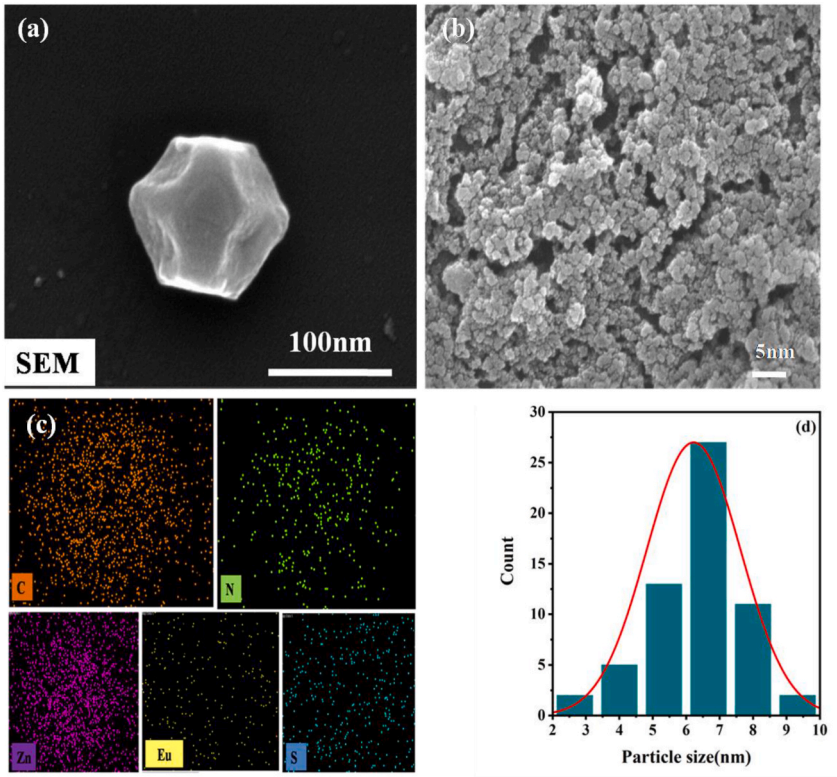

Fig. 5. (a) SEM and (c) EDX mapped images of the ZnS:Eu@ZIF-8 complex dodecahedra with the particle size of 335 nm; (b) TEM images of ZnS:Eu QDs and (d) nanoparticle size distribution of ZnS:Eu QDs.

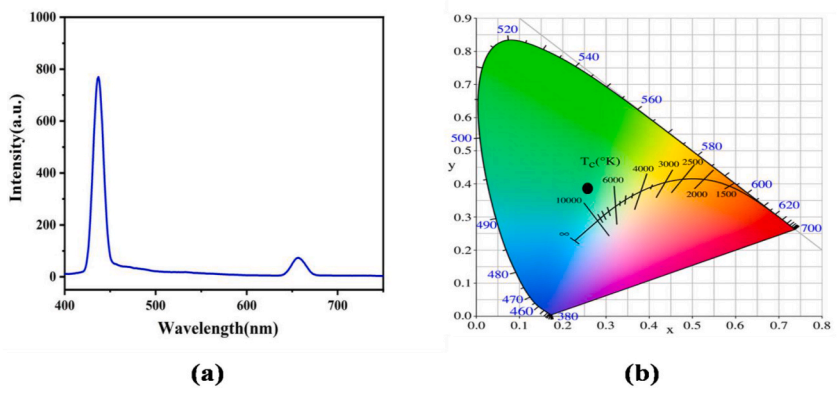

Fig. 6. (a) PL spectra of ZnS:Eu@ZIF8 QDs; (b) CIE of ZnS:Eu@ZIF-8.

blue fluorescence, the material has applications as a luminescent material for the highly sensitive visualisation and detection of photosensitive materials [45].

3.6. Fluorescence sensing of TNP

We investigated the effect of TNP on the luminescent properties of the synthesised fluorescent material. As shown in Fig. 7(a), the characteristic emission peak of Zn ions at 437 nm decreased with the increase in TNP concentration, and the characteristic emission peak of Eu ions at 658 nm decreased similarly. The fluorescence burst efficiency ($F^0_{437}/F^0_{689} - F_{437}/F_{658}$), where $I_{Zn} = 437$ and $I_{Eu} = 658$, was used to calculate the intensity change I_0/I. Fig. 7(b) shows that the best-fit linear equation was $F^0_{437}/F^0_{658} - F_{437}/F_{658} = 0.01853C + 0.06556$ with the correlation coefficient $R^2 = 0.992$. The limit of detection (LOD = 3σ/K) was 0.19 μM. The LOD of TNP was assessed by using equation 3σ/K, where σ is the standard deviation of the repeated assays of the blank probe samples, and k is the

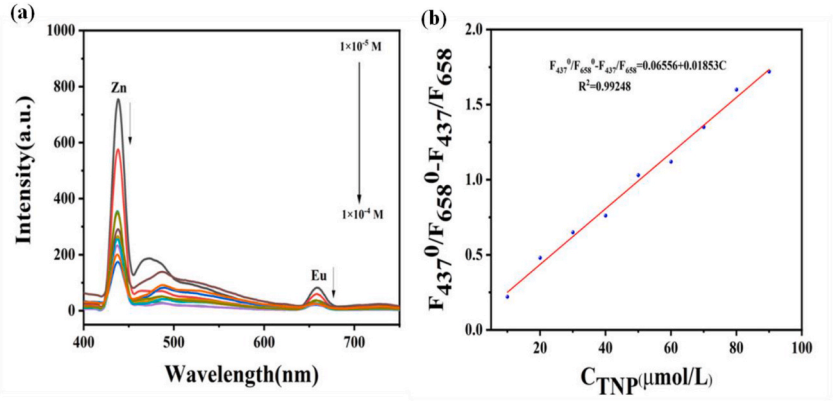

Fig. 7. (a) Fluorescence emission spectra of ZnS:Eu@ZIF-8 spiked with different concentrations of TNP. (b) Calibration line of TNP content (range 10–100 μmol/L).

slope of the linear fit.

3.7. Anti-interference ability of the ratiometric fluorescent sensor

Similarly, we investigated the effect of various interfering metal ions (Cu^{2+}, Ca^{2+}, Ni^{2+}, Zn^{2+}, K^{+}, Na^{+} and Cd^{2+}) on the double-ratio fluorescent sensor ZnS:Eu@ZIF-8 by preparing equal amounts of ZnS:Eu@ZIF-8 powders as suspensions of the same concentration then immersing them into a 1×10^{-4} mol/L TNP solution. The change in their fluorescence intensity is shown in Fig. 8(a), which shows that, except for TNP, the sensor showed no significant change in response to other metal ions. This result indicated that when the TNP solution was added, the luminescence intensity of ZnS:Eu@ZIF-8 underwent a significant sudden extinction. By contrast, when the same concentration of TNP solution was added to the metal ion solution mentioned above, the interfering ions did not interfere with the fluorescence sensor. The ZnS:Eu@ZIF-8 double-ratio fluorescence sensor was observed to be highly selective for the detection of TNP, and the mechanism of this sensing system can be attributed to the internal filtration effect (IFE). As shown in Fig. 8 (b), We also compared the effects of analogues of TNP (3-nitrophenol, *o*-nitroaniline, PHE, 3,5-Dinitrobenzoic acid, DNP, BHA and TBHQ) formulated at the same concentration of 100 μmol/L on the fluorescence intensity of ZnS:Eu@ZIF-8. The graph shows that only TNP had a significant effect on the fluorescence of the fluorescent probe, and by detecting cations and some small molecules, it can be shown that specific identification of TNP detection.

3.8. Effect of pH on the ratiometric fluorescent sensor

We explored the effect of pH values ranging from 5.0 to 9.0 and different reaction times on the ratiometric fluorescent probe to obtain the best experimental protocol. Fig. 9(a) shows that the fluorescence intensity was the strongest when the pH was 6. Therefore, when TNP was added at this pH value, the fluorescence intensity showed the greatest reduction, and the detection effect was the most obvious. Therefore, the pH of 6 was chosen as the best detection condition. The effect of reaction time is illustrated in Fig. 9(b). In the first 2 min, the fluorescence intensity decreased substantially and then showed no significant change. The experiment was therefore carried out after 2 min, which was considered the optimal reaction time.

3.9. Mechanistic studies

The interaction mechanism of ZnS:Eu@ZIF-8 with TNP is discussed. As shown in Fig. 10(a). The UV–vis absorption spectrum of TNP and the fluorescence emission spectrum of ZnS:Eu@ZIF-8 were first obtained to investigate the possible mechanism of the sudden inactivation of ZnS:Eu@ZIF-8 by TNP. In accordance with the dipole–dipole nonradiative energy transfer theory proposed by Förster, and in a phenomenon that also suggested that competitive adsorption occurs between TNP and ZnS:Eu@ZIF-8, a large spectral overlap existed between the fluorescence emission spectrum of ZnS:Eu@ZIF-8 and the UV–Vis absorption spectrum of TNP. Therefore, IFE and resonance energy transfer can be speculated to exist between ZnS:Eu@ZIF-8 and TNP. Fig. 10(b) shows the fluorescence lifetime decay curve of the complex. The ZnS:Eu@ZIF-8 complex showed multiexponential decay. In addition, the average lifetime of Zn:Eu@ZIF-8 decreased from 19.62 ns to 15.43 ns after the addition of TNP during this process. Therefore, in addition to IFE, the detection mechanism in the system may involve dynamic bursting. We speculated that a large number of negatively charged functional groups on the double-ratio fluorescent probe formed hydrogen bonds with the hydroxyl groups in the TNP structure, which greatly increased the bursting efficiency of the fluorescence. As shown in Table 2, the analytical method used in this experiment had similar or higher sensitivity than the methods reported in the literature[46, 47, 48 , 49]. The MOF-based dual-ratio fluorescent sensor constructed here has the advantages of good selectivity and low detection limits and is suitable for the detection and analysis of real samples.

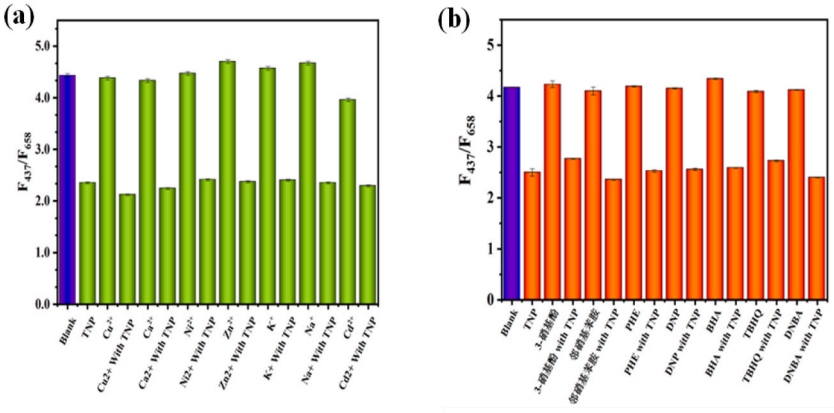

Fig. 8. Effect of (a) different metal ions and (b) organic small molecules on the fluorescence intensity of ZnS:Eu@ZIF-8

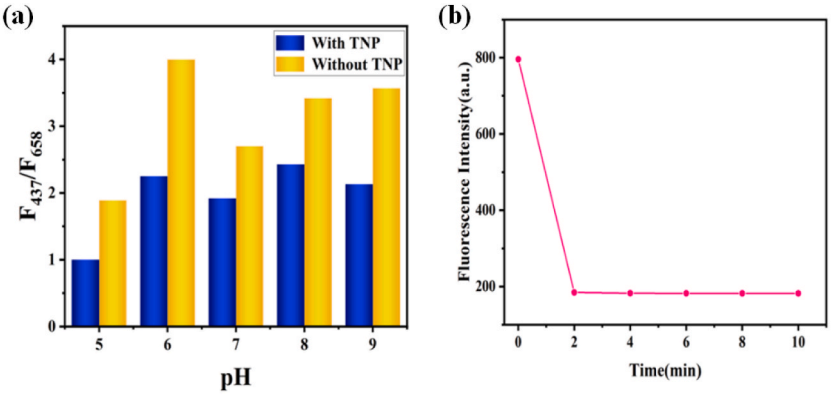

Fig. 9. (a) Fluorescence response of ZnS:Eu@ZIF-8 in the presence and absence of TNP. (b) Fluorescence response of ZnS:Eu@ZIF-8 in the absence and presence of TNP at different incubation times.

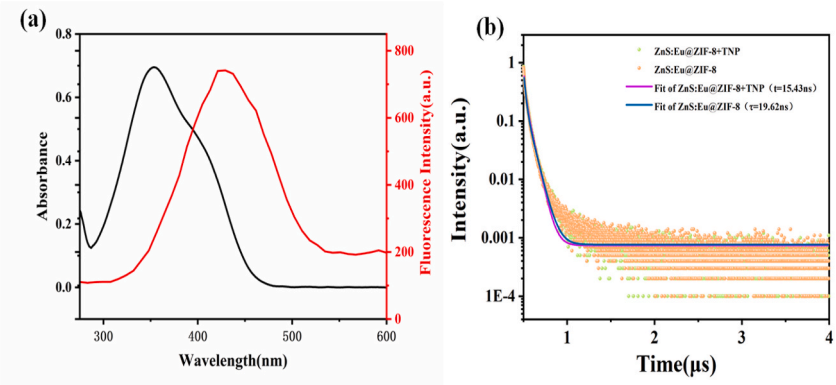

Fig. 10. (a) UV–vis absorption spectrum of TNP (red line) and fluorescence emission spectrum of ZnS:Eu@ZIF-8 (black line). (b) Time-resolved fluorescence spectra of ZnS:Eu@ZIF-8 in the presence and absence of TNP. (For interpretation of the references to color in this figure legend, the reader is referred to the Web version of this article.)

3.10. Application in actual water samples

We further evaluated the feasibility of using the ratiometric ZnS:Eu@ZIF-8 fluorescent probe for the detection of actual samples. The results are provided in Table 3. Applied recovery experiments were carried out at four different concentrations. The recovery rates after the standard addition reached 97.95%–108.5%, and the relative standard deviation was less than 5%. These findings showed that

Table 2
Comparison of the TNP detection performances of different methods.

Testing methods	Linear ranges	Detection limit	References
Capillary electrophoresis	5.0×10^{-9}–1.0×10^{-7} (mol/L)	1.0×10^{-9}(M)	[46]
Chromatography	–	0.16 ($ng.ml^{-1}$)	[47]
Ion migration method	–	30 (nM)	[48]
Fluorescence (MOFL-TpBD)	0.01 ~ 1 (mM)	3.52 (μM)	[49]
ZnS:Eu@ZIF-8	10 ~ 100 (μM)	0.19 (μM)	This Work

the method achieved good recovery and precision and proved that the probe can be used for the determination of TNP in water samples.

Fig. 11 shows the schematic of the preparation and TNP detection processes of ZnS:Eu@ZIF-8. The experimental results illustrated that the addition of TNP caused a significant decrease in the fluorescence intensity of ZnS:Eu@ZIF-8 at 437 nm. The burst effect of Eu in this double-ratio fluorescent sensor^{3+} could be attributed to the interaction between the metal ion and the organic ligand. IFE is one of the causes of the concentration effect (i.e. the decrease in fluorescence intensity with the increase in solution concentration), wherein solute interactions form dimers or complexes, and the overlap between the emission and absorption spectra of fluorescent substances results in the reabsorption of emitted fluorescence [50].

4. Conclusions

In this experiment, a ratiometric fluorescent probe was synthesised via the one-pot method, and the experimental encapsulation of ZnS:Eu (different contents of Eu) into a metal–organic backbone (ZIF-8) was performed. The Eu ion concentration of 4% maximised fluorescence intensity and was used for de-encapsulation with QDs and TNP detection. TNP could effectively reduce the fluorescence intensity of ZnS:Eu@ZIF-8 via the IFE mechanism. On the basis of the IFE mechanism, the intensity of the characteristic fluorescence emission peaks of Zn^{2+} and Eu^{3+} in the ratiometric fluorescence sensor decreased with the increase in TNP concentration, and the ratio of the emission fluorescence intensity at the two wavelengths was linearly related to the concentration of the target. Good linearity was obtained in the range of 0.1–100 μmol/L with a LOD of 0.19 μM under optimal conditions.

In summary, in this work, we developed a novel fluorescence assay that combined dynamic and static quenching between ZnS:Eu QDs@ZIF-8 composites and TNP. The prepared ZnS:Eu QDs@ZIF-8 exhibited good selectivity and sensitivity for TNP. Furthermore, the doped ZnS:Eu QDs were not only less toxic than other QDs, but they also had the advantage of good suitability for proportional fluorescence. The simple fabrication and low cost of ZnS:Eu QDs@ZIF-8 proved the applicability of the method in the determination of TNP.

We propose a method for embedding highly luminescent doped QDs into a MOF, wherein exceptionally small nanoparticles were caged in a cubic sodium structure due to the unique photophysical and chemical properties of the QDs, such as enhanced light absorption, abundant surface binding sites and large surface area.

In addition, ZnS:Eu@ZIF-8 exhibited excellent fluorescence properties on the basis of QDs emission. In this work, in an approach that could potentially be used for the design and application of materials for the detection of specific substances/medicine and environmental-related parameters, the QDs were easily stabilised by certain surfactants or even ions. We then used aspects of the stabiliser and solvent to optimise material morphology and properties and achieved good control of quantum size.

Data availability statement

The authors are unable or have chosen not to specify which data has been used.

Author contribution statement

Qian Wang： Conceived and designed the experiments， Performed the experiments， Analyzed and interpreted the data， Wrote the paper.

Hongtao Chu： Analyzed and interpreted the data， Contributed reagents, materials, analysis tools or data.

Jingru Zhang ： Analyzed and interpreted the data.

Wenhui Ma： Contributed reagents, materials， analysis tools or data.

Shili Qin： Conceived and designed the experiments，Contributed reagents, materials, analysis tools or data.

Table 3
Determination of TNP in real samples (n = 3).

Sample	Spiked (nM)	Found (nM)	Recovery (%)	RSD (%)
Tap water	1	0.98	98.77	3.71
	5	5.23	104.60	3.79
	10	10.85	108.50	4.28
	20	19.59	97.95	4.62

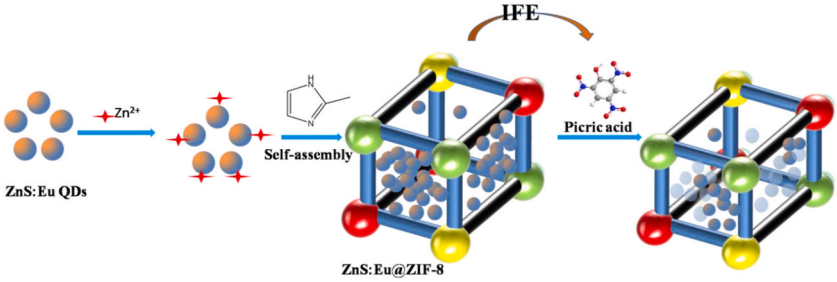

Fig. 11. Schematic of ZnS:Eu@ZIF-8 preparation and application in TNP detection.

Lidi Gao： Conceived and designed the experiments.

Declaration of competing interest

The authors declare that the research was conducted in the absence of any commercial or financial relationships that could be construed as a potential conflict of interest.

References

[1] F.Y. Yi, D. Chen, M.K. Wu, et al., Chemical sensors based on metal-organic frameworks, ChemPlusChem (2016) 81.
[2] S. Ma, Gas Adsorption Applications of Porous Metal-Organic frameworks, Miami University., 2008.
[3] G. Lu, S. Li, Z. Guo, et al., Imparting functionality to a metal-organic framework material by controlled nanoparticle encapsulation, Nat. Chem. 4 (4) (2012) 310.
[4] D. Buso, J. Jasieniak, M. Lay, et al., Highly Luminescent Metal-Organic Frameworks through Quantum Dot Doping, Small, 2012.
[5] D. Esken, S. Turner, C. Wiktor, et al., GaN@ZIF-8: selective formation of gallium nitride quantum dots inside a zinc methylimidazolate framework, J. Am. Chem. Soc. 133 (41) (2011) 16370–16373.
[6] L. Giri, R. Dandela, S.R. Rout, et al., Recent advancements in metal–organic frameworks integrating quantum dots (QDs@MOF) and their potential applications, Nanotechnol. Rev. 11 (1) (2022) 1947–1976.
[7] J. Hafizovic, M. Rgen, U. Olsbye, et al., The inconsistency in adsorption properties and powder XRD data of MOF-5 is rationalized by framework interpenetration and the presence of organic and inorganic species in the nanocavities, J. Am. Chem. Soc. 129 (12) (2007) 3612.
[8] G. Lu, S. Li, Z. Guo, et al., Imparting functionality to a metal-organic framework material by controlled nanoparticle encapsulation, Nat. Chem. 4 (4) (2012) 310.
[9] H. Chu, D. Yao, J. Chen, et al., Double-emission ratiometric fluorescent sensors composed of rare-earth-doped ZnS quantum dots for Hg $^{2+}$ detection, ACS Omega 5 (16) (2020) 9558–9565.
[10] S. Tomar, S. Gupta, S. Mukherjee, et al., Manganese-doped ZnS QDs: an investigation into the optimal amount of doping, Semiconductors 54 (11) (2020) 1450–1458.
[11] M.S. Sannaikar, L.S. Inamdar, G.H. Pujar, et al., Comprehensive study of interaction between biocompatible PEG-InP/ZnS QDs and bovine serum albumin, Luminescence 33 (3) (2017) 495.
[12] X. Ma, Z. Yu, J. Song, Fabrication of strong brightness water-soluble ZnS and ZnS:Mn quantum dots, Sci. Adv. Mater. 2 (2) (2010) 219–222.
[13] H. Chu, D. Yao, J. Chen, et al., Double-emission ratiometric fluorescent sensors composed of rare-earth-doped ZnS quantum dots for Hg 2+ detection, ACS Omega 5 (16) (2020) 9558–9565.
[14] Y. Gong, H. Wu, Z. Fan, Water-soluble Eu(III)-doped ZnS quantum dots for the room-temperature phosphorescence detection of melamine in milk products, Anal. Methods 5 (21) (2013) 6114–6119.
[15] H. Zhu, Z. Gan, D. Li, et al., Sensitive detection of dopamine with ultrasound cavitation-enhanced fluorescence method, Microchem. J. 150 (2019), 104199.
[16] D. Zhu, W. Li, H.M. Wen, et al., Self-assembled Mn-doped ZnSe quantum dot-methyl viologen nanohybrids as an OFF-ON fluorescent probe for time-resolved fluorescence detection of tiopronin, Anal. Methods 5 (2013).
[17] H. Blom, L. Kastrup, C. Eggeling, Fluorescence fluctuation spectroscopy in reduced detection volumes, Curr. Pharmaceut. Biotechnol. 7 (1) (2006) 51–66.
[18] Y. Gong, H. Wu, Z. Fan, Water-soluble Eu(III)-doped ZnS quantum dots for the room-temperature phosphorescence detection of melamine in milk products, Anal. Methods 5 (21) (2013) 6114–6119.
[19] I. Smal, M. Loog, W. Niessen, et al., Quantitative comparison of spot detection methods in fluorescence microscopy, IEEE Trans. Med. Imag. 29 (2) (2010) 282–301.
[20] K. Wang, L. Wang, W. Jiang, et al., A sensitive enzymatic method for paraoxon detection based on enzyme inhibition and fluorescence quenching, Talanta 84 (2) (2011) 400–405.
[21] Y. Shu, Q. Ye, T. Dai, et al., Encapsulation of luminescent guests to construct luminescent metal-organic frameworks for chemical sensing, ACS Sens. 6 (3) (2021).
[22] Dengyu Pan, Jingchun Zhang, Zhen Li, et al., Hydrothermal route for cutting graphenesheets into blue-luminescent graphene quantum dots, Adv. Mater. 22 (6) (2010) 734–738.
[23] A. Tiwari, S.A. Khan, R.S. Kher, et al., Thermoluminescence characteristics of inorganically and organically capped ZnS:Cu nanophosphors, J. Lumin. 131 (10) (2011) 2202–2206.
[24] X. Ma, Z. Yu, J. Song, Fabrication of strong brightness water-soluble ZnS and ZnS:Mn quantum dots, Sci. Adv. Mater. 2 (2) (2010) 219–222.
[25] Devulapalli, Amaranatha, Reddy, et al., Tunable blue-green-emitting wurtzite ZnS:Mg nanosheet-assembled hierarchical spheres for near-UV white LEDs, Nanoscale Res. Lett. 9 (2014) 20.
[26] Y. Peng, Y.W. Wang, Z.H. Fu, Two fluorescein-based chemosensors for the fast detection of 2,4,6-trinitrophenol (TNP) in water, Chem, Commun 53 (2017) 10524–10527, https://doi.org/10.1039/C7CC05966C.
[27] Jinshui Liu, Fangfei Wu, Ao Xie, Chenfu Liu, Huijuan Bao, Preparation of nonconjugated fluorescent polymer nanoparticles for use as a fluorescent probe for detection of 2,4,6-trinitrophenol, Anal. Bioanal. Chem. 412 (5) (2020).
[28] R. Batool, N. Riaz, H.M. Junaid, et al., Fluorene-based fluorometric and colorimetric conjugated polymers for sensitive detection of 2,4,6-trinitrophenol explosive in aqueous medium, ACS Omega 7 (2022) 1057–1070.
[29] H. Harms, T. Bosma, Mass transfer limitation of microbial growth and pollutant degradation, J. Ind. Microbiol. Biotechnol. 18 (2–3) (1997) 97–105.
[30] S.F. Simoni, H. Harms, T. Bosma, et al., Population heterogeneity affects transport of bacteria through sand columns at low flow rates, Environ. Sci. Technol. 32 (14) (1998) 2100–2105.

[31] E.A. Goidl, T. Hayama, G.M. Shepherd, et al., Production of auto-anti-idiotypic antibody during the normal immune response to TNP-ficoll. II. Hapten-reversible inhibition of anti-TNP plaque-forming cells by immune serum as an assay for auto-anti-idiotypic antibody, J. Immunol. Methods 58 (1–2) (1983) 1–17.
[32] E. Claassen, N. Kors, N.V. Rooijen, Influence of carriers on the development and localization of anti-2,4,6-trinitrophenyl (TNP) antibody-forming cells in the murine spleen: II. Suppressed antibody response to TNP-Ficoll after elimination of marginal zone cells, Eur. J. Immunol. 16 (5) (1986).
[33] D.N. Sauder, K. Tamaki, A.N. Moshell, et al., Induction of tolerance to topically applied TNCB using TNCB-conjugated ultraviolet light-irradiated epidermal cells, J. Immunol. 127 (1) (1981) 261–265.
[34] R.A. Miller, O. Stutman, Decline, in aging mice, of the anti-2,4,6-trinitrophenyl (TNP) cytotoxic T cell response attributable to loss of Lyt-2-, interleukin 2-producing helper cell function, Eur. J. Immunol. 11 (10) (1981) 751–756.
[35] C.O. Elson, K.W. Beagley, A.T. Sharmanov, et al., Hapten-induced model of murine inflammatory bowel disease: mucosa immune responses and protection by tolerance, J. Immunol. 157 (5) (1996) 2174–2185.
[36] B. Poornaprakash, S.V. Vattikuti, K. Prabhakar Subramanyam, Cheruku Rajesh, Devarayapalli Kamakshaiah Charyulu, Y.L. Kim, Minnam Reddy Vasudeva Reddy, Herie Park, Pratap Reddy M. Siva, Photoluminescence and hydrogen evolution properties of ZnS:Eu quantum dots, Ceramics Int. 47 (20) (2021).
[37] X. Xue, C. Lei, C. Zhao, et al., One-pot synthesis of highly luminescent and color-tunable water-soluble Mn:ZnSe/ZnS core/shell quantum dots by microwave-assisted method, J. Mater. Sci. Mater. Electron. 29 (11) (2018) 9184–9192.
[38] Y.R. Lee, M.S. Jang, H.Y. Cho, et al., ZIF-8: a comparison of synthesis methods, Chem. Eng. J. 271 (2015) 276–280.
[39] L.M. Zhou, L.J. Gao, S.M. Fang, G.H. Sun, M. Hu, L.Q. Guo, C. Han, L.C. Zhang, Preparation and characterization of noveltransparent Eu(AA)3-polyurethane acrylate copolymeric materials, J. Appl. Polym. Sci. 125 (2012) 690–696.
[40] L.J.T. Hupp, Metal-organic frameworks as sensors: a ZIF-8 based Fabry-Pérot device as a selective sensor for chemical vapors and gases, J. Am. Chem. Soc. 132 (23) (2010) 7832.
[41] D. Fairen-Jimenez, S.A. Moggach, M.T. Wharmby, et al., Opening the gate: framework flexibility in ZIF-8 explored by experiments and simulations, J. Am. Chem. Soc. 133 (23) (2011) 8900–8902.
[42] U. Tran, K. Le, N. Phan, Expanding applications of metal-organic frameworks: zeolite imidazolate framework ZIF-8 as an efficient heterogeneous catalyst for the knoevenagel reaction, ACS Catal. 1 (2) (2011) 120–127.
[43] M. OrdonEz, K.J. Balkus, J.P. Ferraris, et al., Molecular sieving realized with ZIF-8/Matrimid mixed-matrix membranes, J. Membr. Sci. 361 (1–2) (2010) 28–37.
[44] L.D. Sun, C.H. Yan, C.H. Liu, C.S. Liao, D. Li, J.Q. Yu, J. Alloys Compd. 234 (1998) 275–277.
[45] K.A. Fedorova, G.S. Sokolovskii, M. Khomylev, et al., Efficient yellow-green light generation at 561nm by frequency-doubling of a QD-FBG laser diode in a PPLN waveguide, Opt Lett. 39 (23) (2014) 6672–6674.
[46] J.H. Li, D.Z. Kuang, Y.L. Feng, et al., Preparation of TNP electrochemical sensor based on Silver;Nanoparticles/graphene oxide nanocomposite, Chin. J. Inorg. Chem. 29 (6) (2013) 1157–1164.
[47] J.D. Moore, J.P. Sommadossi, Determination of O-(chloroacetylcarbamoyl)fumagillol (TNP-470; AGM-1470) and two metabolites in plasma by high-performance liquid chromatography/mass spectrometry with atmospheric pressure chemical ionization, J. Mass Spectrom. 30 (12) (1995) 1707–1715.
[48] A. Uzer, R. Apak, O.K. Koc, High quantum yield nitrogen-doped carbon quantum dot-based fluorescent probes for selective sensing of 2,4,6-trinitrotoluene, ACS Appl. Nano Mater. 5 (4) (2022) 5868–5881.
[49] W.T. Li, Z.J. Hu, J. Meng, et al., Zn-based metal organic framework-covalent organic framework composites for trace lead extraction and fluorescence detection of TNP, J. Hazard Mater. 411 (2021), 125021.
[50] S. Chen, Y.L. Yu, J.H. Wang, Inner filter effect-based fluorescent sensing systems: a review, Anal. Chim. Acta 999 (2018) 13–26.